

# Multiscalar Investigation of FeVO<sub>4</sub> Conversion Cathode for a Low Concentration Zn(CF<sub>3</sub>SO<sub>3</sub>)<sub>2</sub> Rechargeable Zn-Ion Aqueous Battery

Sonal Kumar<sup>+</sup><sup>[a]</sup> Vivek Verma<sup>+</sup><sup>[a]</sup> Rodney Chua,<sup>[a]</sup> Hao Ren,<sup>[a]</sup> Pinit Kidkhunthod,<sup>[b]</sup> Catleya Rojviriya,<sup>[b]</sup> Suchinda Sattayaporn,<sup>[b]</sup> Frank M. F. de Groot,<sup>[c]</sup> William Manalastas, Jr.,<sup>[a]</sup> and Madhavi Srinivasan<sup>\*[a, d]</sup>

Battery cathode materials operating on multivalent-ion intercalation are prone to short operational lifetimes, traditionally explained to be due to poor solid-state diffusion. Here, we overcome this problem by using a conversion-type cathode material and demonstrate the benefits in a FeVO<sub>4</sub> host structure. The rechargeable Zn-ion battery exhibits stability for an unprecedented operational lifetime of 57 days with a high capacity of 272 mAhg<sup>-1</sup> (60 mA g<sup>-1</sup>) over 140 cycles. We use a combination of synchrotron-based XAS, SRXTM, Raman, XRD

and HRTEM techniques to elucidate the cathode material evolution at multilength-scale for understanding the Zn-ion storage mechanism. We further highlight the benefits of using a low-salt concentration electrolyte and pH-consideration analysis in aqueous battery development, the optimization of which leads to a 4-fold increase in battery performance as compared to conventional high-salt concentration electrolyte formulations.

## 1. Introduction

Rapidly rising energy demands and resultant environmental concerns have directed battery research towards exploring 1) non-lithium chemistries owing to their high abundance, low cost, and high volumetric capacity<sup>[1–8]</sup> and 2) water as an electrolyte solvent owing to superior ionic conductivity and lower desolvation penalty for the charge-transfer process occurring at the electrode-electrolyte interface.<sup>[9]</sup> The use of an aqueous solvent opens new opportunities for high rate capabilities, non-toxicity and non-flammability, and therefore imply safer batteries at low cost.<sup>[10–15]</sup> In this scheme of things, zinc-ion aqueous batteries (ZIAB) are particularly interesting because of the high stability of Zn metal (as anode) in water

and its low redox potential which makes the anodic stripping/plating of Zn feasible without significant electrolytic decomposition.<sup>[16]</sup>

However, the primary challenge lies in developing cathode materials that can reversibly store Zn ions. Most of the cathode materials reported so far show reversible Zn<sup>2+</sup> storage via intercalation mechanisms and are restricted to mostly a few families of materials such as MnO<sub>2</sub> polymorphs, vanadium-based oxides and Prussian Blue Analogues.<sup>[2,17]</sup> The high charge-to-size ratio of Zn<sup>2+</sup> diminishes its cation diffusivity in the host structure and can also induce a heavy structural distortion leading to the collapse of the host structure.<sup>[18–19]</sup> Reversibly storing cations might be less problematic in a conversion-type host materials where cation storage proceeds through thermodynamically favorable reactions, thus avoiding the sluggish insertion kinetics.<sup>[20]</sup> Until now, very few conversion-type cathode materials have been explored including VS<sub>4</sub>/rGO,<sup>[21]</sup> Mn<sub>3</sub>O<sub>4</sub>,<sup>[22]</sup> VN<sub>0.9</sub>O<sub>0.15</sub>,<sup>[23]</sup> and α-MnO<sub>2</sub>; among which α-MnO<sub>2</sub> reaction mechanism is still unclear.<sup>[24–28]</sup> Hence, it is worth exploring traditional conversion-type materials for Zn<sup>2+</sup> storage and understand the concomitant storage mechanism.

In this study, we investigate FeVO<sub>4</sub> as a potential cathode material for ZIAB and elucidate the charge-storage mechanism. Although FeVO<sub>4</sub> has been previously demonstrated as a cathode material in multivalent systems such as Mg<sup>2+</sup> & Al<sup>3+</sup>,<sup>[29–31]</sup> either the cation storage mechanism was not fully elucidated, or parasitic side reactions obscured the true cation storage mechanism. Investigating FeVO<sub>4</sub> is particularly interesting because: 1) it has two redox centers, namely, Fe and V, both of which can be electrochemically reduced to accommodate a large amount of reacting cation, 2) FeVO<sub>4</sub> is electrochemically active in a wide potential range (0.02–3.5 V vs. Li<sup>+</sup>/

[a] S. Kumar,<sup>+</sup> V. Verma,<sup>+</sup> R. Chua, Dr. H. Ren, Dr. W. Manalastas, Jr., Prof. M. Srinivasan

School of Materials Science and Engineering  
Nanyang Technological University  
50 Nanyang Ave 639798, Singapore

[b] Dr. P. Kidkhunthod, Dr. C. Rojviriya, Dr. S. Sattayaporn  
Synchrotron Light Research Institute (SLRI)  
Nakhon Ratchasima 30000, Thailand

[c] Prof. F. M. F. de Groot  
Inorganic Chemistry & Catalysis,  
Debye Institute for Nanomaterials Science  
Utrecht University-99,  
3584 CG Utrecht, Netherlands

[d] Prof. M. Srinivasan  
Energy Research Institute at Nanyang Technological University  
Research Techno Plaza, 50 Nanyang Drive,  
Singapore 637553, Singapore  
E-mail: madhavi@ntu.edu.sg

[+] These authors contributed equally to this work.

 Supporting information for this article is available on the WWW under  
<https://doi.org/10.1002/batt.202000018>

Li), making it appropriate for the electrochemical studies within the stability window of water,<sup>[32–33]</sup> and 3) FeVO<sub>4</sub> has been demonstrated to react with monovalent,<sup>[34]</sup> bivalent,<sup>[29]</sup> and trivalent ions,<sup>[31]</sup> which makes it versatile and apt for applications where more than one aliovalent cation needs to react simultaneously.

We demonstrate that FeVO<sub>4</sub> can deliver a capacity of nearly 180 mAh g<sup>-1</sup> for 300 cycles at a high current rate of 3 A g<sup>-1</sup> and with an average discharge voltage of 0.6 V (vs. Zn<sup>2+</sup>/Zn). To obtain the best performance of the FeVO<sub>4</sub> cathode material at slower current rates however, we show that electrolyte pH has an important role to play. Using a simple technique to make the electrolyte less acidic just by reducing the salt concentration in the electrolyte, we demonstrate an improved capacity retention from 18% to 78.8% in the first 50 cycles. Using this optimized electrolyte, the FeVO<sub>4</sub>-Zn battery was fabricated, and a combination of in-house and synchrotron-based techniques were used to elucidate the Zn-ion reaction mechanism with FeVO<sub>4</sub>. The storage mechanism was found to be conversion-type, and various phases forming during the electrochemical reactions were identified. As some reaction products were amorphous, techniques sensitive to short-range order such as Raman and X-ray absorption spectroscopy (XAS) were also used. Finally, the bulk evolution of the electrode was also elucidated at submillimetre scale using synchrotron-radiation X-ray tomographic microscopy (SRXTM), which shows a reversible material reorganization at the micron scale observed in the form of reversibly formed ridges/valley features and increasing/decreasing porosity in the material upon cycling.

## 2. Results and Discussion

### 2.1. Characterization of FeVO<sub>4</sub> Nanorods

Figure 1a shows the XRD pattern of the synthesized powder which was fitted by refining the  $P\bar{1}$  space group Ziminaite phase and matches well with the triclinic FeVO<sub>4</sub> structure reported by Robertson et al. (PDF no- 01-071-1592) (Full refinement details in Table S1).<sup>[35]</sup> The resultant lattice parameters were calculated to be  $a=6.714(1)$  Å,  $b=8.066(1)$  Å,  $c=9.352(1)$  Å,  $\alpha=96.68(1)$ °,  $\beta=106.67(1)$ °,  $\gamma=101.53(1)$ °, similar to a previous report.<sup>[31]</sup> The absence of any impurity peaks in the XRD pattern confirms that the synthesized material has a single crystalline phase. The FeVO<sub>4</sub> crystal structure consists of Fe atoms in three different coordination environments of oxygen. Both Fe1 and Fe3 centers (Figure 1b) form distorted FeO<sub>6</sub> octahedra with six unequal Fe–O bonds. On the other hand, Fe2 forms a distorted trigonal bipyramidal with the oxygen atoms. Finally, the three V centers form distorted tetrahedra with the oxygen atoms and only share corners with the adjacent Fe polyhedra.

SEM and TEM micrographs for synthesized powder (Figure 1c & 1d) show a predominantly high aspect ratio rod-like morphology with an average length and diameter of 4.7 μm and 290 nm, respectively. The SEM micrograph also features few seed-like particles expected to be FeVO<sub>4</sub> nucleation points which had not grown fully during the synthesis because of insufficient reaction time. The HRTEM image (Figure 1e) shows a fringe spacing of 0.42 nm and 0.32 nm and could be ascribed to the *d*-spacing of the (102) and (022) planes of the FeVO<sub>4</sub> crystal structure, respectively. TEM-EDX elemental mapping

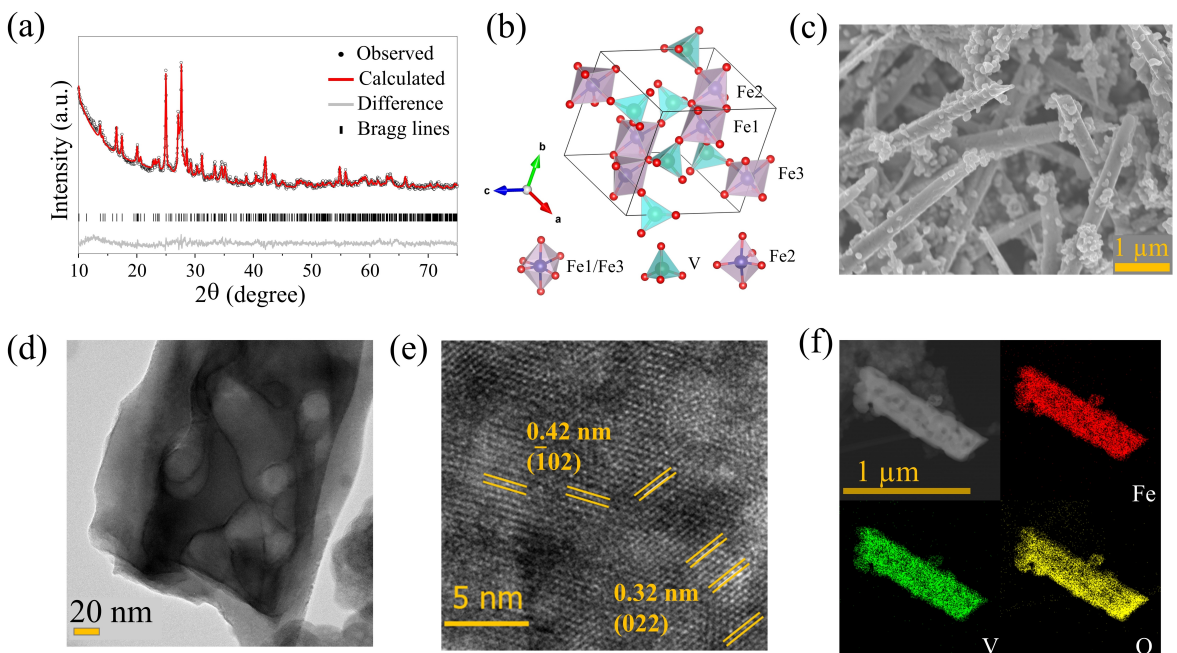


**Figure 1.** Structural characterization of the synthesized FeVO<sub>4</sub> powder: a) Experimental XRD pattern fitted with Rietveld refined Ziminaite phase, b) FeVO<sub>4</sub> unit cell showing the coordination environments of Fe and V. Morphology characterization of the FeVO<sub>4</sub> powder: c) SEM micrograph, d) TEM micrograph, e) HRTEM image, and f) TEM-EDX elemental mappings for Fe, V and O of the FeVO<sub>4</sub> nanorod.

(Figure 1f) shows a homogenous distribution of Fe, V and O in the synthesized  $\text{FeVO}_4$  powder and no other elemental impurity was detected in the TEM-EDX energy spectra (Figure S1).

## 2.2. Electrochemical Activity

Cyclic voltammetry (CV) was used to evaluate the electrochemical activity of  $\text{FeVO}_4$ -Zn system in  $0.1 \text{ M Zn}(\text{CF}_3\text{SO}_3)_2$  (ZnTFS) aqueous electrolyte. The 1<sup>st</sup> negative sweep in the CV profile (Figure 2a) shows the presence of one sharp and one broad cathodic peak occurring at 0.62 V and 0.30 V, respec-

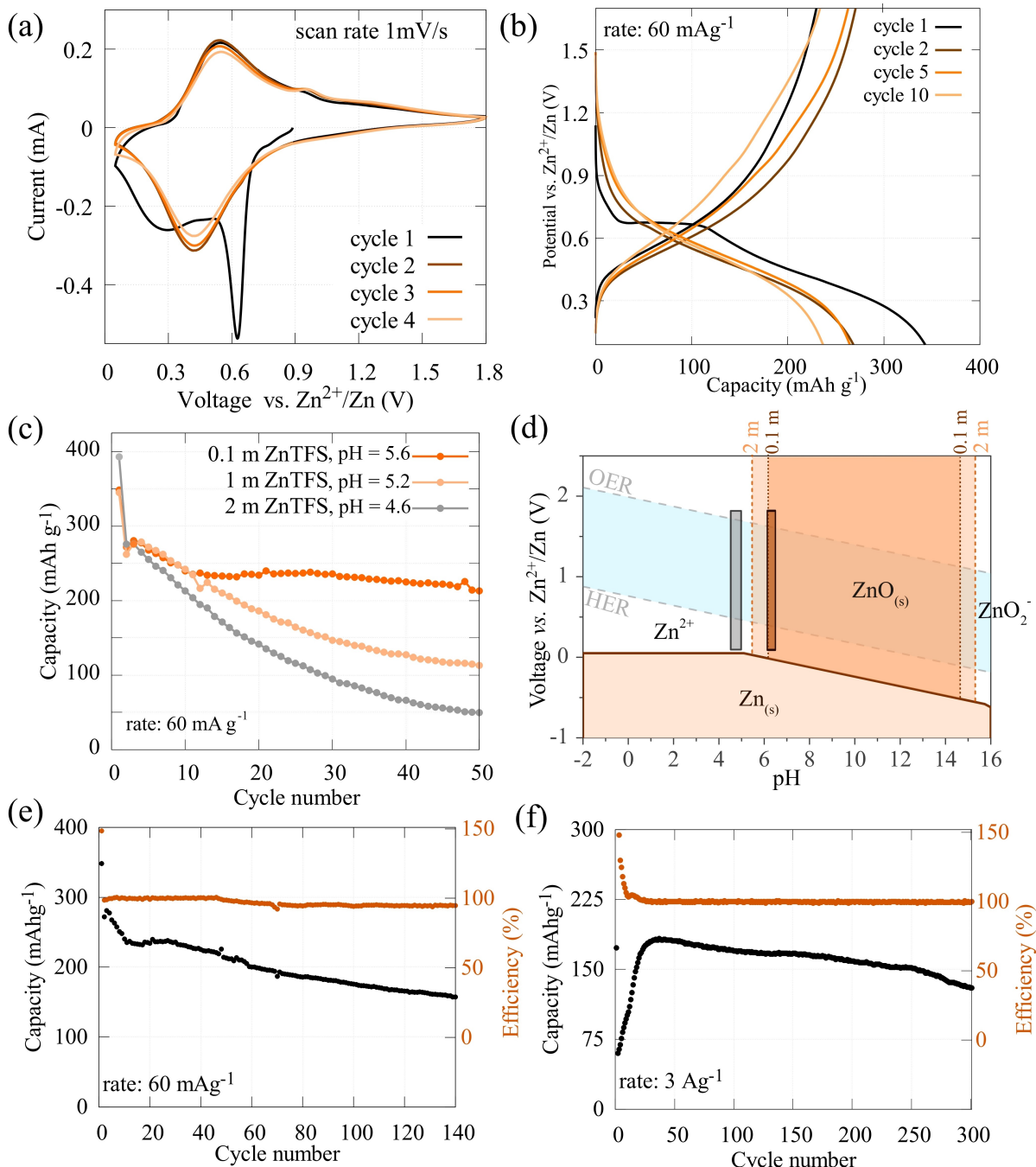


**Figure 2.** Electrochemical activity of the  $\text{FeVO}_4$ : a) Cycling voltammograms in the  $0.1 \text{ M ZnTFS}$  between  $0.05 \text{ V}$  and  $1.8 \text{ V}$  vs.  $\text{Zn}^{2+}/\text{Zn}$ , at scan rate of  $1 \text{ mV s}^{-1}$ , b) Galvanostatic charge/discharge profiles in  $0.1 \text{ M ZnTFS}$  electrolyte between  $0.05 \text{ V}$  to  $1.8 \text{ V}$  vs.  $\text{Zn}^{2+}/\text{Zn}$ , c) Cycling stability of  $\text{FeVO}_4$ -Zn system in three different electrolytes with varying ZnTFS salt concentration, and d) The Pourbaix diagram of Zn/water system (developed using data guidelines from)<sup>[50-51,90]</sup> depicting the thermodynamically stable states of zinc species in two different aqueous solutions with  $[\text{Zn}^{2+}] = 0.1 \text{ M}$  and  $2 \text{ M}$ . Brown and grey rectangles highlight the operating voltage and pH region for  $\text{FeVO}_4$ -Zn cells cycled in  $0.1 \text{ M}$  and  $2 \text{ M}$  ZnTFS electrolytes, respectively. Extended cycling performance and corresponding coulombic efficiency at e)  $60 \text{ mA g}^{-1}$  and f)  $3 \text{ A g}^{-1}$ .

tively. However, only one anodic peak was observed at 0.55 V in the 1<sup>st</sup> positive sweep, indicating only one cathodic reaction to be reversible. Similar irreversibility in the first cycle has also been observed for the Li<sup>+</sup> and K<sup>+</sup>-FeVO<sub>4</sub> systems previously.<sup>[34,36]</sup>

The galvanostatic charge-discharge (GCD) study (Figure 2b) concurs with the observations made in the CV study. Corresponding to the sharp cathodic peak at 0.62 V and broad cathodic peak at 0.3 V in the CV, the 1<sup>st</sup> discharge profile shows a flat plateau at ~0.65 V followed by a gradual sloping profile. This plateau feature has also been observed in the conversion-type transition metal oxides for Li-ion systems,<sup>[37–40]</sup> and was ascribed to a two-phase reaction (see section 2.5 for details).<sup>[39,41]</sup> Notably, subsequent charge or discharge cycles do not show the presence of any plateau feature, indicating that the irreversible reactions

occur only in the first discharge step. This irreversibility is also reflected in terms of the drastic drop in discharge capacity from ~348 mAh g<sup>-1</sup> in 1<sup>st</sup> cycle to ~272 mAh g<sup>-1</sup> in the 2<sup>nd</sup> cycle (Figure 2b). Based on CV and GCD studies, we find that the electrochemical behavior of the FeVO<sub>4</sub>-Zn system resembles a conversion-type storage mechanism where an irreversible reaction occurring in first cycle leads to a high first discharge capacity, and reversible reactions follow in the subsequent cycles.<sup>[20]</sup>

### 2.3. Electrolyte Optimization

Numerous works have demonstrated high cycling stability and high capacity retention at fast cycling rates for ZIAB systems.<sup>[2,17]</sup> However, few investigations have reported that the capacity fading is much higher at slower cycling rates or longer cycling runtimes.<sup>[42–43]</sup> This has been ascribed to the acidic nature of the electrolytes used in the ZIAB system.<sup>[2,44]</sup> Specifically, the active material or the reaction products formed during charge/discharge are susceptible to dissolve in the electrolyte when the electrodes are cycled in acidic pH conditions.<sup>[2,45]</sup> One possible solution to curb this problem can be to increase the electrolyte pH and make the electrolyte less acidic.<sup>[2,31,46]</sup> We demonstrate that electrolytes can be made less acidic by reducing the salt concentration. The measured pH values for three ZnTFS/water electrolytes with salt concentrations of 0.1 m, 1 m and 2 m were 5.6, 5.2 and 4.6, respectively. The difference in the pH values can be explained by the difference in the free H<sup>+</sup> concentration of the solution. The Zn<sup>2+</sup>-ions in the aqueous solution exist as [Zn(H<sub>2</sub>O)<sub>6</sub>]<sup>2+</sup> octahedral complexes.<sup>[47]</sup> Since the Zn<sup>2+</sup> ion center can act as Lewis acid, it can strongly polarize the coordinated water molecules to give H<sup>+</sup>.<sup>[48]</sup> At high salt concentrations, a higher number of Zn<sup>2+</sup> (or [Zn(H<sub>2</sub>O)<sub>6</sub>]<sup>2+</sup>) species in the aqueous medium will result in an increased concentration of H<sup>+</sup>, thus making the solution more acidic. A similar trend of decreasing pH value with increasing salt concentration was also observed in the ZnSO<sub>4</sub>/water system.<sup>[46]</sup>

To test the effect of the electrolytes pH on the cycling performance of FeVO<sub>4</sub>-Zn system, we ran galvanostatic charge-

discharge tests for the three cases (Figure 2c). While the 2<sup>nd</sup> discharge capacity is nearly the same for all three systems, the capacity fading over subsequent cycles follow the trend: 2 m > 1 m > 0.1 m. The system with 0.1 m ZnTFS/water outperforms the other two systems with a high capacity retention of 78.8%, against 43.1% and 18.8% for 1 m and 2 m concentration, respectively, in the first 50 cycles.

This observed disparity in the cycling stabilities can be explained by using a potential vs. pH diagram, Pourbaix diagram, which depicts the thermodynamically stable state of a metal-ion in an aqueous medium.<sup>[49]</sup> Figure 2d shows Pourbaix diagram for Zn, showing the different thermodynamically stable state of Zn such as ZnO, Zn<sup>2+</sup>, metallic Zn or ZnO<sup>2-</sup> in two different systems with [Zn<sup>2+</sup>] of 0.1 m and 2 m in an aqueous medium.<sup>[50–51]</sup> Note that the Zn<sup>2+</sup>/ZnO<sub>(s)</sub> boundary and the ZnO<sub>(s)</sub>/ZnO<sup>2-</sup> boundary vary slightly for two different [Zn<sup>2+</sup>].

For FeVO<sub>4</sub>-Zn systems with two different electrolytes: 0.1 m and 2 m ZnTFS/water, we mark the operating voltage-pH region on the Pourbaix diagram and identify the respective stable Zn species. The operating battery voltage for both the systems is in the range 0.05 to 1.8 V vs. Zn<sup>2+</sup>/Zn (the applied voltage), and the operating pH for these two systems was determined by in-operando pH measurements for the first few cycles (Figure S2). The pH values stabilized to ~6.1–6.3 ( $\pm 0.1$ ) and ~4.5–4.9 ( $\pm 0.1$ ) for 0.1 m and 2 m electrolytes, respectively. These two different operating ranges of pH are critical in governing the stability of the ZnO phase which, as we show later in section 2.5, is also the primary phase responsible for storing Zn-ions. While the ZnO phase is stable for the 0.1 m ZnTFS system (brown rectangle), it is unstable in the 2 m ZnTFS electrolyte system (grey rectangle) and can spontaneously dissolve into the electrolyte as Zn<sup>2+</sup>-ions. The lower stability of ZnO phase in the 2 m ZnTFS electrolyte system results in the poor cycling stability (Figure 2c). A similar idea of phase stability/instability, determined using Pourbaix diagram, has been used previously to explain the cycling stabilities in the oxides of Mn, Mo and V.<sup>[45]</sup>

### 2.4. Electrochemical Performance

Long cycling stability was further investigated at slow (60 mA g<sup>-1</sup>) and fast (3 A g<sup>-1</sup>) current rates for two different coin cells (Figure 2e and Figure 2f). At a low current rate of 60 mA g<sup>-1</sup> and after 140 cycles (roughly 57 days of runtime), the battery could still retain a capacity of 156 mAh g<sup>-1</sup> (57.3% of its 2<sup>nd</sup> discharge capacity). To the best of our knowledge, the combination of the observed discharge capacity and capacity retention is one of the best values reported in the aqueous ZIAB systems at such a slow current rate. For the first 100 cycles, we demonstrate a capacity retention of 64.3%, which is on par with one of the best capacity retention of 51.1% demonstrated by Zhang et al. (see Table S2 for comparison with existing reports on ZIAB).<sup>[42]</sup> At a high current rate of 3 A g<sup>-1</sup>, galvanostatic charge-discharge test shows that FeVO<sub>4</sub> can maintain a high capacity of ~180 mAh g<sup>-1</sup> for nearly 300 cycles (Figure 2f). Notably, the initial cycling performance at

two cycling rates do contrast strongly. At a slower cycling rate of  $60 \text{ mAh g}^{-1}$ , the capacity decreases rapidly in the first few cycles. This can be explained by the probable irreversible reactions taking place in the cathode material which is discussed in detail within the main text (sections 2.5–2.6) in terms of the formation of irreversible phases consisting of V and Fe species. On the other hand, at a higher rate of  $3 \text{ Ah g}^{-1}$ , a gradual rise in the capacity is observed. This rise can be ascribed to the gradual activation of ZIB electrodes<sup>[43,52–53]</sup> wherein, due to the high rate of charge/discharge, the reaction of the cathode with  $\text{Zn}^{2+}$  is initially kinetically limited. EIS spectra of the Zn-FeVO<sub>4</sub> system (Figure S3a& b) show this activation phenomenon in terms of higher charge-transfer-resistance at electrode-electrolyte interface for the first few cycles, which later decreases through the 20th cycle, indicating that by the 20<sup>th</sup> cycle the cathode is fully active towards  $\text{Zn}^{2+}$  reaction.

## 2.5. Phase Evolution of FeVO<sub>4</sub> on Zn-Ion Reaction

Ex situ XRD studies were performed on the cycled electrodes to gain insights into the FeVO<sub>4</sub> phase-evolution upon electrochemical reaction with Zn-ions. For the first discharge cycle, three electrodes discharged to different depths of discharge (0.7 V, 0.6 V and 0.05 V; as shown in the inset of Figure 3), were

investigated to study the phase evolution in the first discharge step. Further, XRD patterns of electrodes charged/discharged in the 4<sup>th</sup> cycle (4 C and 4D) and 10<sup>th</sup> cycle (10 C and 10D) were also taken. In the 1<sup>st</sup> discharge cycle, we find that the main FeVO<sub>4</sub> peaks are still present when discharged to 0.7 V and then disappears after the GCD plateau region (in electrode discharged to 0.6 V). This indicates a possibility of FeVO<sub>4</sub> amorphization, which is later confirmed using Raman Spectroscopy (see Section 2.7). This amorphization process occurs through a two-phase reaction and is consistent with the observations made for conversion reactions of transition metal-oxides with Li.<sup>[40–41]</sup> In the subsequent cycles (4C, 4D, 10C, 10D), the characteristic FeVO<sub>4</sub> peaks do not appear back, indicating that the amorphization of FeVO<sub>4</sub> in the first discharge was irreversible, as also observed in Li-FeVO<sub>4</sub> system.<sup>[54]</sup> Additionally, three new phases: ZnO (PDF- 01-083-6338),<sup>[55]</sup> metallic Fe (PDF- 04-017-1577),<sup>[56]</sup> and  $\text{Zn}_3\text{V}_2\text{O}_7(\text{OH})_2 \cdot 2\text{H}_2\text{O}$  (PDF- 00-057-0572),<sup>[57]</sup> were detected in the cycled electrodes as discussed below.

The formation of ZnO phase starts during the appearance of the plateau region in GCD (indicated by the appearance of its main peaks in the electrode discharged until 0.6 V), and continues to form until fully discharged, as indicated by an increase in the ZnO peak intensities (1D). In the subsequent cycles, ZnO disappears in the charged electrodes (4 C and 10 C) and then reappears in the discharged electrodes (4D and 10D); indicating its high reversibility. The formation of ZnO phase

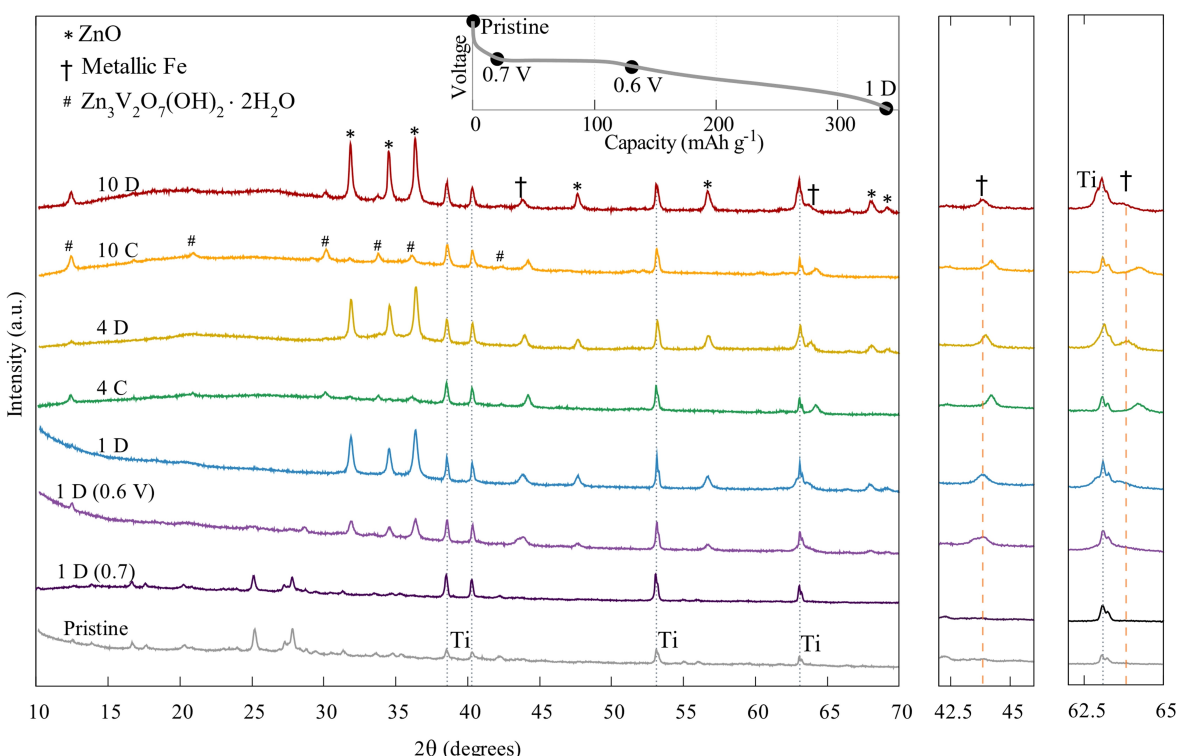


**Figure 3.** Ex situ X-ray diffractograms of the FeVO<sub>4</sub> cathode collected at the different stages of charge/discharge. 1D (0.7 V), 1D (0.6 V) and 1D (full discharge until 0.05 V) are the diffractograms collected at the different voltages during the first discharge, as shown in the inset figure. 4C and 4D are diffractograms taken at the end of the 4<sup>th</sup> cycle in the charged and discharged state, respectively. 10C and 10D are diffractograms taken at the end of 10<sup>th</sup> cycle in the charged and discharged state, respectively. The two figures at the right represent the zoomed-in region of the two metallic Fe peaks, showing the shifts in peak position upon cycling.

was further confirmed by other techniques such as HRTEM, TEM-EDX and XPS analysis, as discussed along with Figure S4 in supplementary.

Metallic Fe phase appears after the appearance of the plateau region, indicating that the metallic Fe is formed in the plateau region during the  $\text{FeVO}_4$  amorphization and  $\text{ZnO}$  formation. The formation of metallic-Fe during the  $\text{FeVO}_4$  amorphization has also been previously observed in the Li- $\text{FeVO}_4$  system.<sup>[54,58]</sup> After the 1<sup>st</sup> discharge step (1D), metallic Fe phase is present in all the subsequent cycles of the  $\text{FeVO}_4\text{-Zn}$  system, indicating that the formation of the metallic Fe is not reversible. When comparing the XRD peak positions of the metallic-Fe phase in charged and discharged electrodes we find that the Fe peaks shift to lower  $2\theta$  angles in the discharged state. Indeed, a Pawley fitting for the discharged (10D) and the charged (10 C) electrode reveals lattice parameter values of  $a = 2.922(1)$  Å and  $2.9090$  (7), respectively. Although the exact reason for the peak shifts is not very clear, only picometer length scale change in the lattice parameter suggests that the possibility of electrochemical alloying of Zn with metallic-Fe is unlikely.<sup>[59–60]</sup>

The third phase detected was,  $\text{Zn}_3\text{V}_2\text{O}_7(\text{OH})_2\cdot 2\text{H}_2\text{O}$  (PDF- 00-057-0572),<sup>[57]</sup> which is layer-type structure wherein, the layers consisting of Zn oxide/hydroxide octahedra and are supported by the  $\text{V}_2\text{O}_5$  pillars and the water molecules (Figure S4d).<sup>[61]</sup> This phase does not appear until discharge to 0.7 V (electrode 1D (0.7 V)) and only appears after the emergence of a plateau region in the 1<sup>st</sup> discharge in electrode 1D (0.6 V). Further, this phase is present in all the subsequent cycles irrespective of the charge/discharge process, indicating its permanent irreversibility. Formation of this phase is expected at pH values higher

than 5,<sup>[57]</sup> and is consistent with the pH of our electrolyte (~ 6.1–6.3). Here we would like to note that the capacity is continuously declining with every cycle even in the later stages of cycling (Figure 2e & 2f). We did ex situ XRD of electrodes charged/discharged for 20 cycles (Figure S3c) to gain insight into this decline. It is observed that the amount of inactive phase ( $\text{Zn}_3\text{V}_2\text{O}_7(\text{OH})_2\cdot 2\text{H}_2\text{O}$ ) side product increases upon repeated cycling which may have occurred because the transformation of the active phases ( $\text{ZnO}$  to Zn) has not occurred 100% reversibly during cycling, i.e. small amounts of the active phase become orphaned as  $\text{Zn}_3\text{V}_2\text{O}_7(\text{OH})_2\cdot 2\text{H}_2\text{O}$  (more details in Figure S3c and its associated caption).

## 2.6. Redox Reactions of Transition Metal Centers

XPS was used to study the oxidation state changes occurring on the Fe and V metal centers during the electrochemical cycling. Figure 4a shows the  $\text{Fe} 2\text{p}_{3/2}$  region of the XPS spectra exhibited during the 4<sup>th</sup> cycle (showing three panels for pristine, discharged (4D) and charged (4 C)). The pristine  $\text{Fe} 2\text{p}_{3/2}$  spectrum was fitted with two model peaks (blue and green), which most likely represent two different coordinating environments of  $\text{Fe}^{3+}$  (trigonal bipyramidal and octahedral; as also discussed in section 2.1).<sup>[32]</sup> Upon discharge, a broad low binding energy peak (705.37 eV) was detected corresponding to the metallic phase of Fe;<sup>[62–64]</sup> consistent with the XRD results. However, no metallic Fe was detected in the XPS spectrum of the charged electrodes, even though XRD results showed that metallic Fe is present (Figure 3). This ambiguity can be because, unlike XRD, XPS is a surface

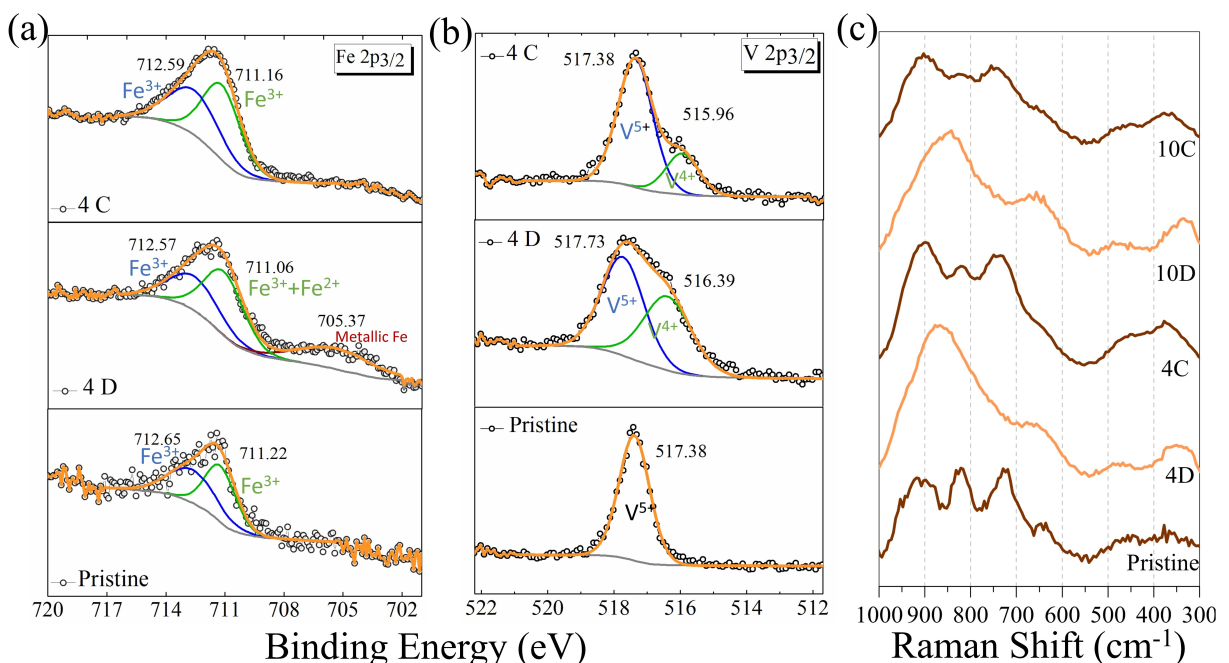


**Figure 4.** a)  $\text{Fe} 2\text{p}_{3/2}$  and b)  $\text{V} 2\text{p}_{3/2}$  region of XPS spectra for pristine, discharged (4D) and charged (4C) electrodes. Open circles: experimental data; grey line: background; blue and green lines: deconvoluted model peaks; orange line: overall fitted spectrum. c) Ex situ Raman spectra for the pristine electrode and the evolution of the spectrum during the 4<sup>th</sup> and 10<sup>th</sup> cycle (electrodes –4D, 4C, 10D and 10C).

technique capable of detecting only a few nm below the surface. It is also observed that the low energy modeled peak (green peak) in the pristine electrode shifts to a lower binding energy value upon discharge (electrode 4D), and that this shift to lower energy is more clearly observed in the 10<sup>th</sup> cycle (Figure S5a, electrode 10D), indicating a partial reduction of the Fe<sup>3+</sup> species to Fe<sup>2+</sup>.<sup>[65]</sup> Upon subsequent charging (electrode 4C), this green model peak recovers back to the original energy value of the pristine sample, indicating that the reduced Fe species oxidizes back to Fe<sup>3+</sup>. Therefore, based from the above observations, we infer that the Fe species in FeVO<sub>4</sub> undergo two kinds of reduction: 1) irreversible Fe<sup>3+</sup> to metallic Fe transformation, which primarily occurs in initial stages of reaction with Zn-ion and 2) reversible Fe<sup>3+</sup> to Fe<sup>2+</sup> reduction/oxidation taking place during the discharge/charge process.

Figure 4b shows the V 2p<sub>3/2</sub> region of XPS spectra for the 4<sup>th</sup> cycle (showing three panels for pristine, discharged (4D) and charged (4C) electrodes). The pristine V 2p<sub>3/2</sub> spectrum was fitted with one model peak (at 517.38 eV) and represents +5 oxidation state.<sup>[66]</sup> Upon discharge, this original peak at 517.38 eV splits into two peaks: 1) higher energy peak (blue model peak), which may correspond to only a slight modification of the local coordination environment of V<sup>5+</sup><sup>[67]</sup> and 2) lower energy peak (green model peak), which indicates reduction of V<sup>5+</sup> to a lower oxidation state. Upon subsequent charging (electrode 4C), the spectra were deconvoluted into two peaks: 1) the peak at ~517.38 eV indicates that the original coordination environment of V is recovered upon charging and 2) the peak at ~515.96 eV (green peak) indicates that a small amount of reduced V<sup>5+</sup> remains irreversibly reduced. Interestingly, the area ratio between the above two peaks (green model peak to blue model peak) remained constant (~25:75) in the 4<sup>th</sup> and 10<sup>th</sup> cycle charged electrode samples- 4C (Figure 4b) and 10C (Figure S5b). This reveals that the amount of irreversibly reduced V is constant and hence this reduction may have taken place along with the formation of irreversible phases like metallic Fe and Zn<sub>3</sub>V<sub>2</sub>O<sub>7</sub>(OH)<sub>2</sub>·2H<sub>2</sub>O in the first discharge step. Based on the above observations we infer that, like Fe, V species in FeVO<sub>4</sub> undergoes two kind of reduction: 1) irreversible reduction speculated to occur in the initial stages of reaction with Zn-ion and 2) reversible reduction/oxidation of V<sup>5+</sup> species during discharge/charge process.

## 2.7. Local Structural Evolution

The Raman spectra for the pristine FeVO<sub>4</sub> powder shows four broad peaks corresponding to different vibration modes (Figure 4c). Raman shifts between: 1) 300 and 550 cm<sup>-1</sup> correspond to V-O-V deformation and Fe-O stretching; 2) 550 to 700 cm<sup>-1</sup> represents a mixed bridging V-O···Fe & V···O···Fe stretching; 3) 700 and 880 cm<sup>-1</sup> are bridging V-O···Fe stretching and 4) 880 to 950 cm<sup>-1</sup> range arise from terminal V-O stretching modes.<sup>[31,68-70]</sup> Upon discharging (4D and 10D): 1) the peak between 300 to 350 cm<sup>-1</sup> shifts to a lower wavenumber and recovers to the original position upon subsequent charging (4C and 10C). This might indicate a reversible expansion in local

crystal lattice upon Zn-ion reaction, as also observed for LiNi<sub>1-x</sub>Co<sub>x</sub>O<sub>2</sub> and Li<sub>x</sub>V<sub>2</sub>O<sub>5</sub>.<sup>[71]</sup> and 2) the high wavenumber peaks in 700 to 1000 cm<sup>-1</sup> range broaden to give rise to a single and broad band centered at ~850 cm<sup>-1</sup>(4D and 10D), which reversibly disbands into original FeVO<sub>4</sub> peaks upon charging (4C and 10C). The Raman spectrum with broad peaks has also been observed for FeVO<sub>4</sub> powder synthesized at various calcination temperatures, wherein the peak broadening phenomenon was more prominent in FeVO<sub>4</sub> calcined at lower temperatures and was ascribed to loss in crystallinity.<sup>[69]</sup> A similar broadening of Raman peaks has also been observed during the Li-ion insertion in V<sub>2</sub>O<sub>5</sub>.<sup>[72]</sup>

Further, even though the overall spectrum differs between the discharged (4D and 10D) and the charged electrodes (4C and 10C), the spectrum for the charged electrodes appears very similar to the pristine electrode. This indicates that the original short-range ordering in the crystalline FeVO<sub>4</sub> is modified upon discharging and recovers back upon subsequent charging, even though the XRD results suggesting a permanent loss in the long-range order. The Raman study provides sufficient proof that the amorphous-FeVO<sub>4</sub> participates in the Zn-ion storage mechanism, and we use XAS technique to study the coordination environments of Fe and V centers.

Figure 5 shows the X-ray absorption near-edge structure spectra (XANES) of Fe and V K-edges which provide information on their local coordination environments and electronic structures.<sup>[73]</sup> A comparative study was done on pristine, discharged and charged electrodes. The pristine Fe K-edge shows the presence of three absorption peaks noted as- A, B, and C (Figure 5a and 5b), as also observed in other Fe K-edge XAS studies.<sup>[31,74-75]</sup> Peak A corresponds to a local electronic transition from Fe 1s to Fe 3d states.<sup>[76]</sup> Peak B, located ~4.5 eV higher than peak A, corresponds to a similar but non-local 1 s to 3d transition also referred to as an intersite hybrid.<sup>[77-78]</sup> Such a transition occurs due to electronic excitation of a 1 s electron from the absorbing metal center (Fe) to 3d states of the next-nearest-neighboring Fe (here denoted as Fe'). Since this transition occurs through Fe(4p)-O(2p)-Fe'(3d) hybridization, peak B is sensitive to the Fe-O-Fe' bond geometry, including angle & length and the coordination number of the absorbing site-Fe.<sup>[75,78]</sup> Finally, peak C (the rising edge) represents the excitation from the 1 s core state to the 4p conduction band of Fe.<sup>[76]</sup>

The following observations are made from the Fe K-edge XANES spectra (Figure 5b): 1) Upon discharging, peak C shifts to lower energy values and recovers back upon charging. This shift of ~0.8 eV to lower energy indicates the reduction of Fe<sup>3+</sup>. Notably, this reduction may have occurred partially in the bulk as a downward energy shift of 4 eV is expected for the complete reduction of Fe<sup>3+</sup> to Fe<sup>2+</sup>.<sup>[79]</sup> 2) The peak A intensity increases upon discharge and reverts back to its original intensity upon charging. This increase in intensity indicates a distortion in the inversion symmetry of the Fe coordination environment (originally present as distorted octahedra), which would have resulted from local 3d-4p mixing, imparting a dipolar nature to this electronic transition.<sup>[76]</sup> 3) The peak B intensity irreversibly diminishes upon discharge, indicating the

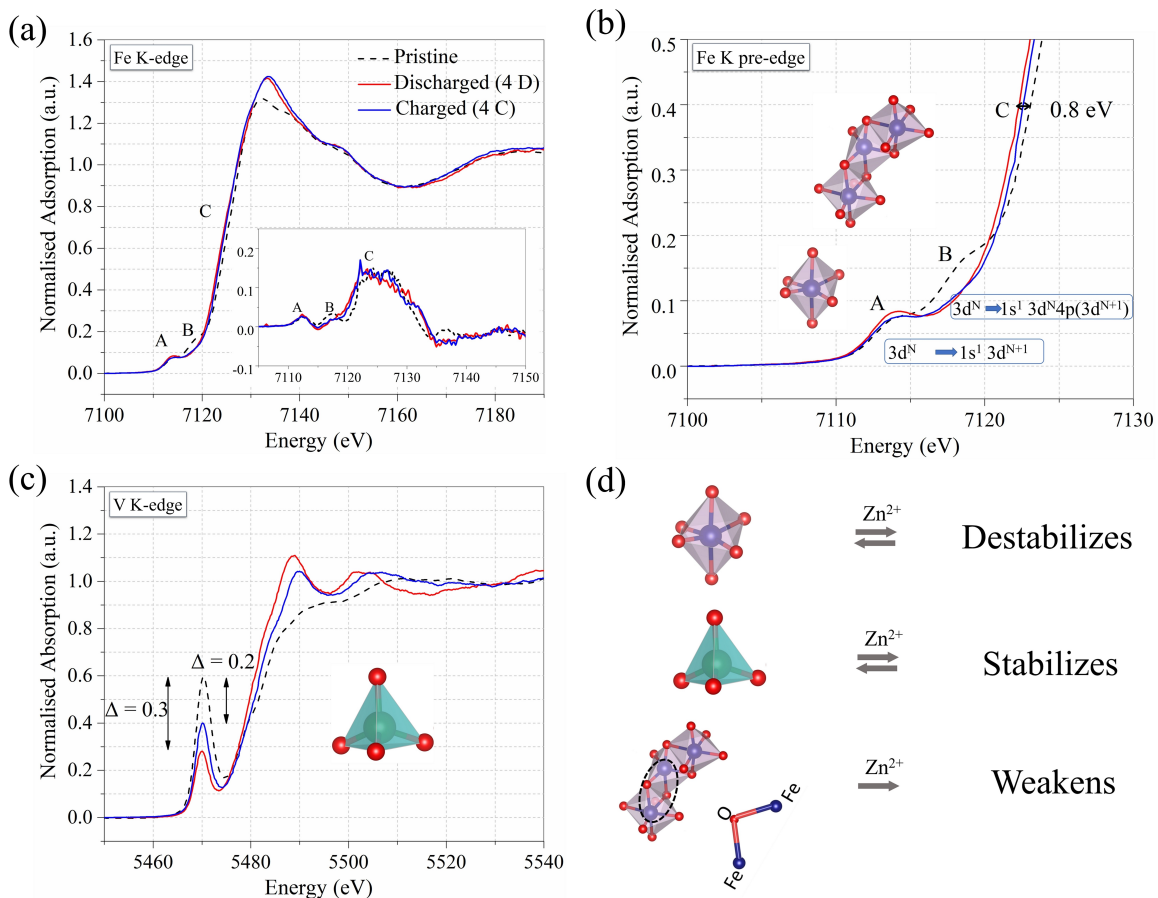


**Figure 5.** Local structural study of the pristine, discharged (4D) and charged (4C) electrodes: a) Background subtracted and normalized XANES spectra for the Fe K-edge (inset: the first derivative curve of XANES spectra for better identification of pre-edge peaks). b) Zoomed in XANES spectra for the Fe K-edge showing the change in the pre-edge intensities and the shift in rising edge upon cycling, c) background subtracted and normalized XANES spectra for the V K-edge showing the change in the pre-edge intensity and the shift in rising edge upon cycling, and d) summary of local structural changes upon Zn intake/ removal.

absence of the unoccupied next-nearest-neighbor 3d state to the Fe atom. This effectively indicates the formation of a new phase wherein the Fe-O-Fe' bond is absent/weak or the modified coordination of Fe where Fe(4p)-O(2p)-Fe'(3d) hybridization is no more possible, unlike FeVO<sub>4</sub>. Similar observations were made by Jessica et al. in terms of diminished non-local/intersite excitations when the concentration of Ga was increased in Fe<sub>1-x</sub>Ga<sub>x</sub>SbO<sub>4</sub>.<sup>[78]</sup>

Regarding V K-edge, XANES spectra of the pristine sample shows one pre-edge feature, indicative of the presence of a tetrahedral environment,<sup>[80-81]</sup> along with the main rising edge (Figure 5c) as also observed by Hellier et al. for FeVO<sub>4</sub>.<sup>[82]</sup> It is observed that: 1) The intensity of the pre-edge peak decreases upon discharge and recovers partially on charging. The reduction in the intensity during discharge indicates an increase in the local symmetry of the vanadium environment.<sup>[81,83]</sup> Such an increase in the symmetry primarily occurs during the conversion of some tetrahedral symmetry to octahedral.<sup>[84]</sup> 2) The rising edge shifts reversibly to lower energy indicating a reduction in the V oxidation state during the discharge.<sup>[80]</sup>

In summary (Figure 5d), upon Zn-ion intake, the local structure of Fe destabilizes by losing its inversion symmetry; the local structure of V stabilizes by becoming more symmetrical; and Fe-O-Fe band breaks/weaken irreversibly. This observation concurs with the idea of Fe and V metal centers of amorphous-FeVO<sub>4</sub> participating in the discharge reaction, as also indicated in XPS and Raman studies.

## 2.8. 3D Morphological Evolution of FeVO<sub>4</sub>

SRXTM study supports a conversion-type mechanism occurring in the FeVO<sub>4</sub> material and gives a visual idea of the development of new phases upon Zn-ion cycling in FeVO<sub>4</sub> at submillimeter length-scales. A comparative study is done on pristine, discharged and charged electrodes (Figure 6). All electrodes exhibit two regions of x-ray attenuating phases: high absorption for the deep material (colored in red) and low absorption for the surface material (colored in blue). SRXTM relies on differences in elemental composition, densities and pathlength considerations to achieve absorption contrast. Notably, the air absorbs x-rays as well, but the majority of its

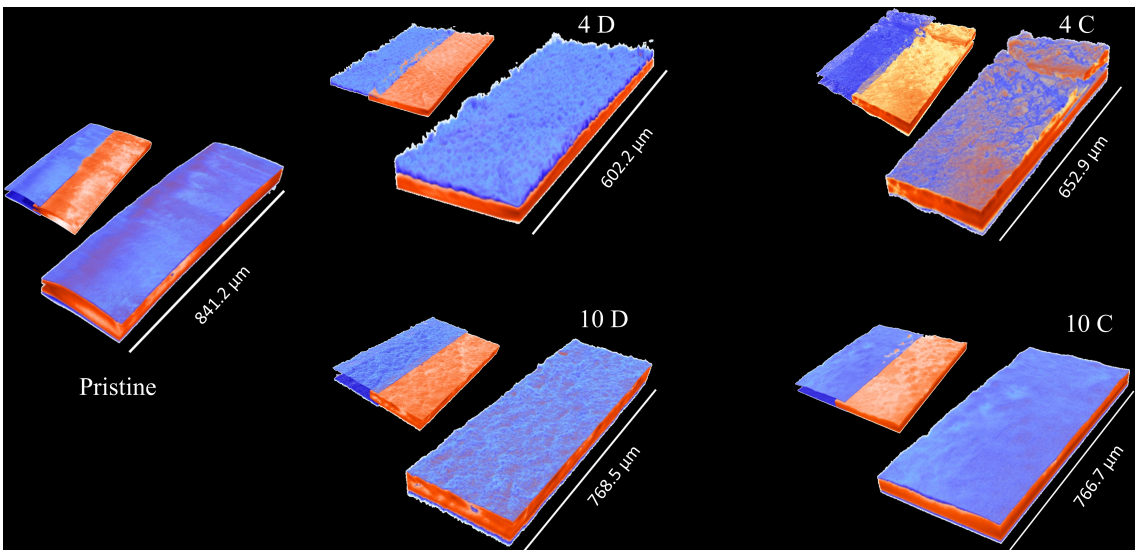


**Figure 6.** Representative tomography images of pristine, 4D, 4C, 10C and 10D electrode showing morphological evolution in electrode upon discharge-charge. Blue and red colors represent low and high X-ray attenuating phases, respectively. The smaller figures adjacent to the electrodes represent the sectioned blue and red-colored phases in respective cases.

contribution has been nullified for these images by careful selection of transference function cut-offs.

The maximum X-ray absorption for point-volumes within the pristine cathode laminate must originate from the high-atomic-number (or high-density)  $\text{FeVO}_4$  particles. Hence,  $\text{FeVO}_4$  can be mapped in 3D to be constrained within the red-phase region. Quantitatively, however, this red-phase region averages out the contiguous absorption contributions of the composite binder and the conductive carbons due to two technical considerations: (a) the synthesized  $\text{FeVO}_4$  is nanosized and (b) the voxel resolution is limited to 2.88  $\mu\text{m}$ . By globally considering these point-volume averages, we see clearly through SRXTM that for the pristine, discharged and charged electrodes, the heavy materials (or high-density) are localized deep within the electrode material, at least on the maximum 2.88- $\mu\text{m}$  resolution scale. We also observe that the low-atomic-number or low-density regions, if any, which are represented by the blue-colored phase tend to be localized nearer the electrode surface.

As expected, the pristine electrode displays a flat uniform morphology at this juxtaposition scale, as a direct consequence of the electrode fabrication process. Upon discharging (4D), the electrode surface exhibits significant roughening from the formation of ridge/valley-like features throughout the electrode surface, consistent with material electrodeposition. Further, upon charging (4 C), the electrode surface exhibits significant smoothening and regions of non-uniform X-ray attenuation. This roughening/smoothening behavior continues through to the 10<sup>th</sup> charge/discharge cycle (electrode 10D/10C). Porosity analyses further give insight into the bulk material volume expansion. Increased porosity is observed further down the cycle number. (9.9% porosity for the pristine material, 13.9% for 4D, 12.3% for 4C, 15.4% for 10D and 13.2% for 10C). A clear

trend of increased porosity is observed upon discharge, which decreases reversibly upon charging.

All the above observations indicate that the formation of new phases upon discharge is resulting in material reorganization at the micron scale, and not simply on the atomic scale. A clear visual indication of the reversible phases forming at the micron scale presents strong evidence for the conversion-type storage mechanism for Zn-ions.

## 2.9. Reaction Mechanism

Overall, the Zn storage mechanism in the  $\text{FeVO}_4$  host can be summarized as follows: XRD study indicates that after the first discharge,  $\text{ZnO}$  and metallic Fe phases form together with irreversible amorphization of  $\text{FeVO}_4$ . During the subsequent cycling steps, the  $\text{ZnO}$  phase appears/disappears upon discharge/charge, whereas metallic-Fe remains irreversibly reduced in metallic form. Parallelly, an irreversible phase  $\text{Zn}_3\text{V}_2\text{O}_7(\text{OH})_2 \cdot 2\text{H}_2\text{O}$  and a small amount of permanently reduced V also forms in the first cycle discharge. Further, XPS, Raman and XAS studies unanimously show a reversible change in the local coordination and electronic environment of Fe and V metal centers of amorphized- $\text{FeVO}_4$  upon cycling, indicating their participation in Zn-ion storage.

Notably, in our system, only two sources of oxygen exist for  $\text{Zn}^{2+}$ -ions to form its oxide: 1) Oxygen from the amorphous- $\text{FeVO}_4$  matrix and 2) Oxygen from the water used as electrolyte solvent. Since three different studies, namely XPS, XAS and Raman, clearly indicate the participation of Fe and V metal centers in the Zn-ion storage mechanism, we expect the  $\text{ZnO}$  phase to be formed as a result of oxygen donation from the amorphous- $\text{FeVO}_4$  matrix. Such mechanisms have also been commonly observed in the transition metal oxides like

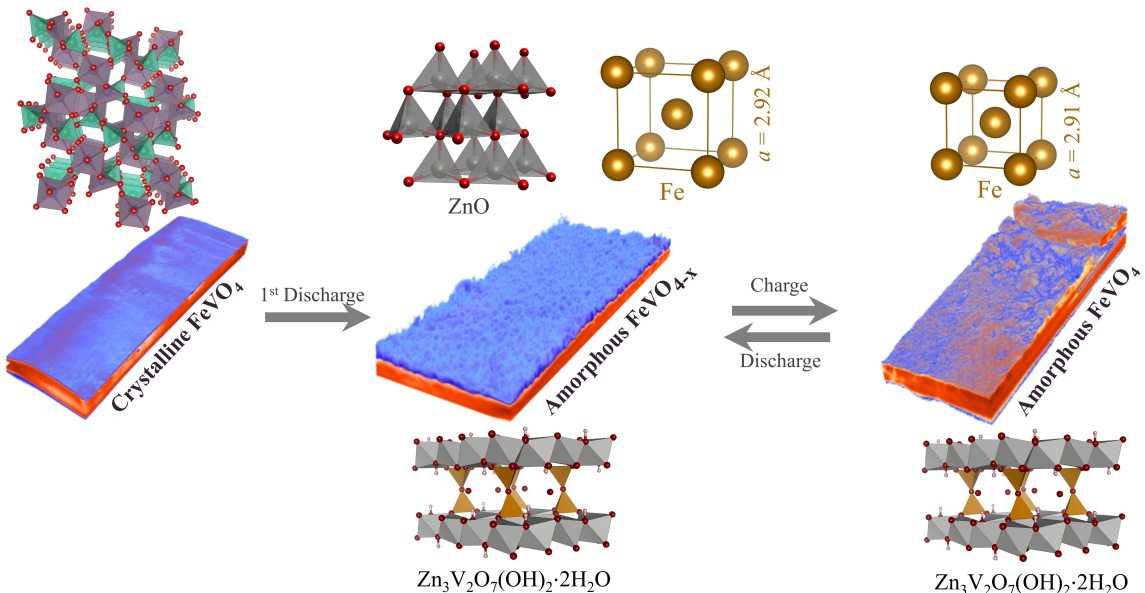


**Figure 7.** The proposed reaction mechanism for reversible Zn-ion storage in the  $\text{FeVO}_4$ : The 1<sup>st</sup> discharge step shows the formation of  $\text{ZnO}$ , metallic-Fe, oxygen-deficient amorphous- $\text{FeVO}_4$  (or  $\text{FeVO}_{4-x}$ ) and  $\text{Zn}_3\text{V}_2\text{O}_7(\text{OH})_2 \cdot 2\text{H}_2\text{O}$ . Hereafter, during charging, the metallic-Fe unit cell volume contracts, the  $\text{ZnO}$  phase disappears, the amorphous- $\text{FeVO}_{4-x}$  gains oxygen ions and  $\text{Zn}_3\text{V}_2\text{O}_7(\text{OH})_2 \cdot 2\text{H}_2\text{O}$  remains irreversibly present; and vice versa during discharging.

$\text{Li}_2\text{MoO}_3$ ,  $\text{Li}_2\text{RuO}_3$  and metal-vanadates reacting with Li.<sup>[41,85–88]</sup> Based on our study, we propose a two-step Zn-ion storage mechanism in  $\text{FeVO}_4$  (Figure 7): 1) In the initial stages of reaction, crystalline  $\text{FeVO}_4$  amorphized along with formation of irreversible phases including  $\text{Zn}_3\text{V}_2\text{O}_7(\text{OH})_2 \cdot 2\text{H}_2\text{O}$ , metallic-Fe and some amount of irreversibly reduced V which accounts for initial loss of capacity and 2) Subsequently, Zn-ion storage takes place by the formation of  $\text{ZnO}$  phase where oxygen-ion is donated by the amorphous- $\text{FeVO}_4$  matrix leading to the formation of oxygen-deficient  $\text{FeVO}_4$  (or  $\text{FeVO}_{4-x}$ ).

### 3. Conclusions

From this study, we highlight two crucial ramifications for multivalent aqueous batteries. Firstly, from the cathode material's perspective, we show that as an alternative to intercalation-type cathode materials, reversibly storing multivalent cations is feasible in conversion-type transition metal oxides in an aqueous electrolyte, and we demonstrate this in a  $\text{FeVO}_4$ -Zn system. Not only can the cathode material demonstrate a high 2<sup>nd</sup> discharge capacity of  $272 \text{ mAh g}^{-1}$  at  $60 \text{ mA/g}$ , but it can also demonstrate a high reversibility of 300 cycles at a high current rate of  $3 \text{ A g}^{-1}$  and retaining a high capacity value of  $\sim 180 \text{ mAh g}^{-1}$ . Further, a combination of complementary characterization techniques including structural investigation at different length scales also highlights a general strategy that can be adopted to study a complex conversion mechanism for other multivalent ions such as  $\text{Mg}^{2+}$ ,  $\text{Ca}^{2+}$  and  $\text{Al}^{3+}$ .

Secondly, from the electrolyte's perspective, we show that the electrolyte pH is a key factor in deciding the cycling stability and the battery lifetime of the system in our case, especially at slower cycling rates or in a longer cycling duration.

We demonstrate a battery with an unprecedented operational lifetime of  $\sim 57$  days. The battery lifetime is particularly important for practical applications in the grid-scale energy storage as frequently replacing the batteries can increase the maintenance cost. Through our study, we have demonstrated that electrolyte pH can be easily increased by reducing the salt concentration of the electrolyte. Contrary to various other studies which use high concentration electrolytes ( $\sim 3 \text{ M}$  ZnTFS),<sup>[28,89]</sup> we show that a  $0.1 \text{ M}$  ZnTFS/water electrolyte outperforms the more concentrated electrolyte system with a high capacity retention of 78.8%, against 18.8% for  $2 \text{ M}$  concentration electrolyte in the first 50 cycles. Reducing the salt concentration from  $2 \text{ M}$  to  $0.1 \text{ M}$  (by 20 times) can reduce the electrolyte cost by 20 times, which has bigger impact when upscaling this technology and is a step towards the commercialization of rechargeable ZIAB.

### Experimental Section

Refer to supporting information for details on experimental section.

### Acknowledgements

This work was financially supported by the National Research Foundation of Singapore (NRF) Investigatorship Award Number NRFI2017-08/NRF2016NRF-NRF001-22. S.K. and V.V. would like to thank Dr. Samuel Morris (NTU, Singapore) for insightful discussions on X-ray diffraction data and Facility for Analysis Characterization Testing and Simulation-NTU, Singapore for the usage of characterization facility. We also thank Dr. Phakkhanan

Pakawanit and Chalermluck Phoovasawat for their assistance in operating synchrotron-beamline stations at SLRI, Thailand; and Dr. Arun Nagasubramanian (TUM-CREATE, Singapore) for fruitful discussions.

## Conflict of Interest

The authors declare no conflict of interest.

**Keywords:** aqueous zinc-ion battery · conversion mechanism · tomography · x-ray absorption spectroscopy · electrolyte pH

- [1] Z. Xing, S. Wang, A. Yu, Z. Chen, *Nano Energy* **2018**, *50*, 229–244.
- [2] V. Verma, S. Kumar, W. Manalastas Jr., R. Satish, M. Srinivasan, *Adv. Sustainable Syst.* **2019**, *3*, 1800111.
- [3] H. Ren, J. Zhao, L. Yang, Q. Liang, S. Madhavi, Q. Yan, *Nano Res.* **2019**, *12*, 1347–1353.
- [4] D. Yuan, W. Manalastas Jr., L. Zhang, J. J. Chan, S. Meng, Y. Chen, M. Srinivasan, *ChemSusChem* **2019**, *12*, 4889–4900.
- [5] J. Zhao, H. Ren, Q. Liang, D. Yuan, S. Xi, C. Wu, W. Manalastas, J. Ma, W. Fang, Y. Zheng, C.-F. Du, M. Srinivasan, Q. Yan, *Nano Energy* **2019**, *62*, 94–102.
- [6] V. Verma, S. Kumar, W. Manalastas Jr., J. Zhao, R. Chua, S. Meng, P. Kidkhunthod, M. Srinivasan, *ACS Appl. Energy Mater.* **2019**.
- [7] G. A. Elia, K. Marquardt, K. Hoeppler, S. Fantini, R. Lin, E. Knipping, W. Peters, J.-F. Drillet, S. Passerini, R. Hahn, *Adv. Mater.* **2016**, *28*, 7564–7579.
- [8] Y. Hu, D. Sun, B. Luo, L. Wang, *Energy Technol.* **2018**, *0*.
- [9] D. Kundu, S. Hosseini Vajargah, L. Wan, B. Adams, D. Prendergast, L. F. Nazar, *Energy Environ. Sci.* **2018**, *11*, 881–892.
- [10] W. Manalastas Jr., S. Kumar, V. Verma, L. Zhang, D. Yuan, M. Srinivasan, *ChemSusChem* **2019**, *12*, 379–396.
- [11] T. Liu, X. Cheng, H. Yu, H. Zhu, N. Peng, R. Zheng, J. Zhang, M. Shui, Y. Cui, J. Shu, *Energy Storage Mater.* **2018**.
- [12] M. R. Lukatskaya, J. I. Feldblum, D. G. Mackanic, F. Lissel, D. L. Michels, Y. Cui, Z. Bao, *Energy Environ. Sci.* **2018**.
- [13] L. Luo, O. Borodin, W. Sun, X. Fan, C. Yang, F. Wang, T. Gao, Z. Ma, M. Schroeder, A. von Cresce, M. Russell Selena, M. Armand, A. Angell, K. Xu, C. Wang, *Angew. Chem. Int. Ed.* **2016**, *55*, 7136–7141; *Angew. Chem.* **2016**, *128*, 7252–7257.
- [14] R. Chua, Y. Cai, Z. K. Kou, R. Satish, H. Ren, J. J. Chan, L. Zhang, S. A. Morris, J. Bai, M. Srinivasan, *Chem. Eng. J.* **2019**, *370*, 742–748.
- [15] D. Yuan, J. Zhao, W. Manalastas, S. Kumar, M. Srinivasan, *Nanomaterials* **2019**.
- [16] X. G. Zhang, Google Patents, **1996**.
- [17] D. Selvakumaran, A. Pan, S. Liang, G. Cao, *J. Mater. Chem. A* **2019**, *7*, 18209–18236.
- [18] Z. Rong, R. Malik, P. Canepa, G. Sai Gautam, M. Liu, A. Jain, K. Persson, G. Ceder, *Chem. Mater.* **2015**, *27*, 6016–6021.
- [19] M. J. Park, H. Yaghobnejad-Asl, S. Therese, A. Manthiram, *J. Mater. Chem. A* **2019**.
- [20] Z. Zhao-Karger, M. Fichtner, *Front. Chem.* **2019**, *6*, 656.
- [21] H. Qin, Z. Yang, L. Chen, X. Chen, L. Wang, *J. Mater. Chem. A* **2018**, *6*, 23757–23765.
- [22] C. Zhu, G. Fang, J. Zhou, J. Guo, Z. Wang, C. Wang, J. Li, Y. Tang, S. Liang, *J. Mater. Chem. A* **2018**, *6*, 9677–9683.
- [23] J. Ding, Z. Du, B. Li, L. Wang, S. Wang, Y. Gong, S. Yang, *Adv. Mater.* **2019**, *31*, 1904369.
- [24] H. Pan, Y. Shao, P. Yan, Y. Cheng, K. S. Han, Z. Nie, C. Wang, J. Yang, X. Li, P. Bhattacharya, K. T. Mueller, J. Liu, *Nat. Energy* **2016**, *1*, 16039.
- [25] C. Xu, B. Li, H. Du, F. Kang, *Angew. Chem. Int. Ed. Engl.* **2012**, *51*, 933–935.
- [26] B. Lee, H. R. Lee, H. Kim, K. Y. Chung, B. W. Cho, S. H. Oh, *Chem. Commun.* **2015**, *51*, 9265–9268.
- [27] B. Lee, C. S. Yoon, H. R. Lee, K. Y. Chung, B. W. Cho, S. H. Oh, *Sci. Rep.* **2014**, *4*, 6066.
- [28] N. Zhang, F. Cheng, J. Liu, L. Wang, X. Long, X. Liu, F. Li, J. Chen, *Nat. Commun.* **2017**, *8*, 405.
- [29] H. Zhang, K. Ye, K. Zhu, R. Cang, J. Yan, K. Cheng, G. Wang, D. Cao, *Electrochim. Acta* **2017**, *256*, 357–364.
- [30] H. Zhang, K. Ye, K. Zhu, R. Cang, J. Yan, K. Cheng, G. Wang, D. Cao, *Chem. Eur. J.* **2017**, *23*, 17118–17126.
- [31] S. Kumar, R. Satish, V. Verma, H. Ren, P. Kidkhunthod, W. Manalastas, M. Srinivasan, *J. Power Sources* **2019**, *426*, 151–161.
- [32] S. Denis, R. Dedryvère, E. Baudrin, S. Laruelle, M. Touboul, J. Olivier-Fourcade, J. C. Jumas, J. M. Tarascon, *Chem. Mater.* **2000**, *12*, 3733–3739.
- [33] S. Patoux, T. J. Richardson, *Electrochim. Commun.* **2007**, *9*, 485–491.
- [34] X. Liu, Y. Cao, H. Zheng, X. Chen, C. Feng, *Appl. Surf. Sci.* **2017**, *394*, 183–189.
- [35] B. Robertson, E. Kostiner, *J. Solid State Chem.* **1972**, *4*, 29–37.
- [36] X. Niu, Y. Zhang, L. Tan, Z. Yang, J. Yang, T. Liu, L. Zeng, Y. Zhu, L. Guo, *Energy Storage Mater.* **2019**.
- [37] P. Poizot, S. Laruelle, S. Grugon, L. Dupont, J. M. Tarascon, *Nature* **2000**, *407*, 496–499.
- [38] P. Balaya, H. Li, L. Kienle, J. Maier, *Adv. Funct. Mater.* **2003**, *13*, 621–625.
- [39] M. Reddy, T. Yu, C.-H. Sow, Z. X. Shen, C. T. Lim, G. Subba Rao, B. Chowdari, *Adv. Funct. Mater.* **2007**, *17*, 2792–2799.
- [40] S.-H. Yu, X. Feng, N. Zhang, J. Seok, H. D. Abruna, *Acc. Chem. Res.* **2018**, *51*, 273–281.
- [41] J. Jang, Y. Kim, O. B. Chae, T. Yoon, S.-M. Kim, H.-s. Kim, H. Park, J. H. Ryu, S. M. Oh, *Angew. Chem. Int. Ed.* **2014**, *53*, 10654–10657; *Angew. Chem.* **2014**, *126*, 10830–10833.
- [42] L. Zhang, I. A. Rodríguez-Pérez, H. Jiang, C. Zhang, D. P. Leonard, Q. Guo, W. Wang, S. Han, L. Wang, X. Ji, *Adv. Funct. Mater.* **2019**, *1902653*.
- [43] M. H. Alfaruqi, V. Mathew, J. Song, S. Kim, S. Islam, D. T. Pham, J. Jo, S. Kim, J. P. Baboo, Z. Xiu, K.-S. Lee, Y.-K. Sun, J. Kim, *Chem. Mater.* **2017**, *29*, 1684–1694.
- [44] R. Demir-Cakan, M. R. Palacín, L. Croguennec, *J. Mater. Chem. A* **2019**.
- [45] S. Boyd, V. Augustyn, *Inorg. Chem. Front.* **2018**, *5*, 999–1015.
- [46] A. S. Poyraz, J. Laughlin, Z. Zec, *Electrochim. Acta* **2019**, *305*, 423–432.
- [47] M. Hartmann, T. Clark, R. van Eldik, *J. Am. Chem. Soc.* **1997**, *119*, 7843–7850.
- [48] C. F. Baes, R. S. Mesmer, *The Hydrolysis of Cations*, 81, John Wiley & Sons Ltd, **1977**, 245–246.
- [49] M. Pourbaix, *Atlas of electrochemical equilibria in aqueous solutions*, Houston, Texas : National Association of Corrosion Engineers, **1974**, 1966.
- [50] B. Beverskog, I. Puigdomenech, *Corros. Sci.* **1997**, *39*, 107–114.
- [51] K. A. Persson, B. Waldwick, P. Lazic, G. Ceder, *Phys. Rev. B* **2012**, *85*, 235438.
- [52] N. Zhang, Y. Dong, M. Jia, X. Bian, Y. Wang, M. Qiu, J. Xu, Y. Liu, L. Jiao, F. Cheng, *ACS Energy Lett.* **2018**, *3*, 1366–1372.
- [53] P. He, G. Zhang, X. Liao, M. Yan, X. Xu, Q. An, J. Liu, L. Mai, *Adv. Energy Mater.* **2018**, *8*, 1702463.
- [54] S. Denis, E. Baudrin, F. Orsini, G. Ouvrard, M. Touboul, J. M. Tarascon, *J. Power Sources* **1999**, *81*–82, 79–84.
- [55] L.-L. Zhao, J.-Y. Wang, X.-L. Wang, Z.-X. Cheng, J. Wang, N. Yin, Z.-G. Gai, A. Jalalian, S.-X. Dou, *J. Alloys Compd.* **2015**, *628*, 303–307.
- [56] G. P. ArneWestgren, *J. Iron Steel Inst. London* **1922**, *105*, 241–273.
- [57] D. Hoyos, L. A. Palacio, J.-L. Paillaud, A. Simon-Masseron, J.-L. Guth, *Solid State Sci.* **2004**, *6*, 1251–1258.
- [58] S. Denis, R. Dedryvere, E. Baudrin, S. Laruelle, M. Touboul, J. Olivier-Fourcade, J. Jumas, J. Tarascon, *Chem. Mater.* **2000**, *12*, 3733–3739.
- [59] G. R. Speich, L. Zwoll, H. A. Wriedt, *Trans. AIME* **1964**, *230*, 939–940.
- [60] A. Grabias, M. Pekala, D. Oleszak, M. Kowalczyk, *J. Magn. Magn. Mater.* **2012**, *324*, 2501–2505.
- [61] P. Y. Zavalij, F. Zhang, M. S. Whittingham, *Acta Crystallogr. Sect. C* **1997**, *53*, 1738–1739.
- [62] A. Lebugle, U. Axelsson, R. Nyholm, N. Mårtensson, *Phys. Scr.* **1981**, *23*, 825–827.
- [63] P. Mills, J. L. Sullivan, *J. Phys. D* **1983**, *16*, 723–732.
- [64] I. N. Shabanova, V. A. Trapeznikov, *J. Electron Spectrosc. Relat. Phenom.* **1975**, *6*, 297–307.
- [65] T. Yamashita, P. Hayes, *Appl. Surf. Sci.* **2008**, *254*, 2441–2449.
- [66] Y. Zhao, K. Yao, Q. Cai, Z. Shi, M. Sheng, H. Lin, M. Shao, *CrystEngComm* **2014**, *16*, 270–276.
- [67] D. Kim, M. Kim, J. Yi, S.-H. Nam, J.-H. Boo, Y. S. Park, J. Lee, *Sci. Adv. Mater.* **2017**, *9*, 1415–1419.
- [68] L. Grazia, D. Bonincontro, A. Lolli, T. Tabanelli, C. Lucarelli, S. Albonetti, F. Cavani, *Green Chem.* **2017**, *19*, 4412–4422.
- [69] A. Š. Vuk, B. Orel, G. Dražić, F. Decker, P. Colombo, *J. Sol-Gel Sci. Technol.* **2002**, *23*, 165–181.

- [70] H. Tian, I.E. Wachs, L. E. Briand, *J. Phys. Chem. B* **2005**, *109*, 23491–23499.
- [71] R. Baddour-Hadjean, J.-P. Pereira-Ramos, *Chem. Rev.* **2010**, *110*, 1278–1319.
- [72] R. Baddour-Hadjean, J. P. Pereira-Ramos, C. Navone, M. Smirnov, *Chem. Mater.* **2008**, *20*, 1916–1923.
- [73] T. E. Westre, P. Kennepohl, J. G. DeWitt, B. Hedman, K. O. Hodgson, E. I. Solomon, *J. Am. Chem. Soc.* **1997**, *119*, 6297–6314.
- [74] F. Liu, H. He, Z. Lian, W. Shan, L. Xie, K. Asakura, W. Yang, H. Deng, *J. Catal.* **2013**, *307*, 340–351.
- [75] F. M. F. de Groot, P. Glatzel, U. Bergmann, P. A. van Aken, R. A. Barrea, S. Klemme, M. Hävecker, A. Knop-Gericke, W. M. Heijboer, B. M. Weckhuysen, *J. Phys. Chem. B* **2005**, *109*, 20751–20762.
- [76] G. Frank de, V. György, G. Pieter, *J. Phys. Condens. Matter* **2009**, *21*, 104207.
- [77] P. Glatzel, A. Mirone, S. G. Eeckhout, M. Sikora, G. Giuli, *Phys. Rev. B* **2008**, *77*, 115133.
- [78] J. A. Sigrist, M. W. Gaulois, A. P. Grosvenor, *J. Phys. Chem. A* **2011**, *115*, 1908–1912.
- [79] W. M. Heijboer, P. Glatzel, K. R. Sawant, R. F. Lobo, U. Bergmann, R. A. Barrea, D. C. Koningsberger, B. M. Weckhuysen, F. M. F. de Groot, *J. Phys. Chem. B* **2004**, *108*, 10002–10011.
- [80] J. Wong, F. W. Lytle, R. P. Messmer, D. H. Maylotte, *Phys. Rev. B* **1984**, *30*, 5596–5610.
- [81] M. Ruitenbeek, A. J. van Dillen, F. M. F. de Groot, I.E. Wachs, J. W. Geus, D. C. Koningsberger, *Top. Catal.* **2000**, *10*, 241–254.
- [82] P. Hellier, P. P. Wells, D. Gianolio, M. Bowker, *Top. Catal.* **2018**, *61*, 357–364.
- [83] K. Palanisamy, J. H. Um, M. Jeong, W.-S. Yoon, *Sci. Rep.* **2016**, *6*, 31275.
- [84] G. S. Henderson, F. M. F. de Groot, B. J. A. Moulton, *Rev. Mineral. Geochem.* **2014**, *78*, 75–138.
- [85] C. H. Kim, Y. S. Jung, K. T. Lee, J. H. Ku, S. M. Oh, *Electrochim. Acta* **2009**, *54*, 4371–4377.
- [86] Y. Shi, B. Guo, S. A. Corr, Q. Shi, Y.-S. Hu, K. R. Heier, L. Chen, R. Seshadri, G. D. Stucky, *Nano Lett.* **2009**, *9*, 4215–4220.
- [87] O. B. Chae, S. Park, J. H. Ryu, S. M. Oh, *J. Electrochem. Soc.* **2013**, *160*, A11–A14.
- [88] J. Wang, N. Yang, H. Tang, Z. Dong, Q. Jin, M. Yang, D. Kisailus, H. Zhao, Z. Tang, D. Wang, *Angew. Chem. Int. Ed.* **2013**, *52*, 6417–6420; *Angew. Chem.* **2013**, *125*, 6545–6548.
- [89] N. Zhang, F. Cheng, Y. Liu, Q. Zhao, K. Lei, C. Chen, X. Liu, J. Chen, *J. Am. Chem. Soc.* **2016**, *138*, 12894–12901.
- [90] A. Jain, S. P. Ong, G. Hautier, W. Chen, W. D. Richards, S. Dacek, S. Cholia, D. Gunter, D. Skinner, G. Ceder, K. A. Persson, *APL Materials* **2013**, *1*, 011002.

Manuscript received: January 24, 2020

Revised manuscript received: February 26, 2020

Version of record online: March 26, 2020